



Geophysical Research Letters*

RESEARCH LETTER

10.1029/2021GL097467

Key Points:

- Infragravity (IG) motions modulate the dynamics of a small river plume in the surfagne
- Outflow velocity, wave breaking intensity and plume salinity all show variability at IG frequencies
- The river plume expands and contracts by 20%–50% at IG frequencies

Supporting Information:

Supporting Information may be found in the online version of this article.

Correspondence to:

R. P. Flores, raul.flores@usm.cl

Citation:

Flores, R. P., Williams, M. E., & Horner-Devine, A. R. (2022). River plume modulation by infragravity wave forcing. *Geophysical Research Letters*, 49, e2021GL097467. https://doi.org/10.1029/2021GL097467

Received 16 DEC 2021 Accepted 5 JUL 2022

Author Contributions:

Conceptualization: Raúl P. Flores,

Megan E. Williams, Alexander R. Horner-Devine
Data curation: Raúl P. Flores, Megan E. Williams, Alexander R. Horner-Devine
Formal analysis: Raúl P. Flores, Megan E. Williams, Alexander R. Horner-Devine
Funding acquisition: Raúl P. Flores
Investigation: Raúl P. Flores, Megan E. Williams, Alexander R. Horner-Devine
Methodology: Raúl P. Flores, Megan E. Williams, Alexander R. Horner-Devine
Project Administration: Raúl P. Flores
Writing – original draft: Raúl P. Flores,
Megan E. Williams, Alexander R.
Horner-Devine

© 2022. American Geophysical Union. All Rights Reserved.

River Plume Modulation by Infragravity Wave Forcing

Raúl P. Flores¹, Megan E. Williams¹, and Alexander R. Horner-Devine²

¹Departamento de Obras Civiles, Universidad Técnica Federico Santa María, Valparaíso, Chile, ²Department of Civil and Environmental Engineering, University of Washington, Seattle, WA, USA

Abstract We present measurements at the mouth of Río Maipo, a small river that discharges into an energetic surfzone on the coast of Chile, which document for the first time the plume response to infragravity (IG) wave forcing. We find that inlet dynamics are strongly modulated by IG waves; inlet discharge velocity varies by 20% in the IG band relative to peak ebb velocity. Drone imaging and measurements of surfzone salinity show that the plume edge is forced offshore and onshore, modifying plume width by 20%–50% at IG frequencies. We conclude that the observed modulation results from surfzone forcing at IG frequencies consistent with a moving break point; increased (decreased) wave amplitude generates stronger (weaker) wave-driven circulation and forces the plume onshore (offshore). Although river water is often trapped in the surfzone, these dynamics may enhance mixing and cross-shore dispersion of river-borne materials.

Plain Language Summary Small coastal rivers often discharge directly into the surfzone, where the fate of river-borne materials such as sediment, nutrients and contaminants is determined by the combined effects of buoyant plume processes, wave-driven dynamics and turbulence. In this work we present field measurements at the mouth of Río Maipo, a small river that discharges into a very energetic surfzone on the coast of central Chile, documenting the response of the plume to infragravity (IG) wave forcing (timescales of 30–300 s) for the first time. We observe persistent velocity and salinity oscillations at IG frequencies when freshwater is leaving the estuary, and that the plume edge is moved onshore and offshore at these frequencies, in response to forcing in the wave breaking region. This work suggests that the IG forcing may influence the dispersion of freshwater and river-borne materials in small river systems subjected to strong wave forcing.

1. Introduction

Small-scale freshwater outflows are common features of coastlines worldwide, particularly at mid-latitudes with Mediterranean climates (e.g., McSweeney et al., 2017). Globally, these systems represent an important source of freshwater, sediments and nutrients to the coastal ocean, with a net contribution that is comparable to that of large river systems (Basdurak et al., 2020; Izett & Fennel, 2018; Milliman & Syvitski, 1992; Syvitski et al., 2003). However, little attention has been given to the processes that determine the fate of river-borne material in small rivers, which are key to understanding the evolution of water quality, coastal morphology and biochemical cycles along adjacent shorelines.

Small river systems often discharge directly into energetic surfzone regions, and the dynamics of these systems are strongly influenced by the nearshore wave forcing. The incoming wave field forces flow in the surfzone via the divergence in the radiation stresses and controls the generation of turbulence in the nearshore (Feddersen, 2012; Longuet-Higgins & Stewart, 1964; Stive & Wind, 1982), with implications for mixing and retention of riverine freshwater (Kastner et al., 2019; Rodriguez et al., 2018). Recent numerical studies have suggested that the nearshore wave forcing and wave breaking can confine discharge from small rivers to the coastline, such that a large part of the freshwater mixing and dilution may happen within short distances from the river mouth (Delpey et al., 2014; Rodriguez et al., 2018). As a consequence, potentially harmful impacts of river waters can be enhanced in areas where human exposure is maximized, particularly in highly urbanized watersheds.

Conceptual models that predict the fate of freshwater in the surfzone use length scales to characterize river and wave momentum, and the presence of alongshore currents (e.g., Kastner et al., 2019; Wong et al., 2013). The three primary length scales are: the surfzone width $(L_{\rm SZ})$, the near-field plume length $(L_{\rm NF})$ and the cross-flow length (L_a) . The near-field plume length is based on discharge momentum (i.e., river velocity) and plume buoyancy, and is given by (Hetland, 2010; Jones et al., 2007; Kastner et al., 2019)

FLORES ET AL. 1 of 12

$$L_{NF} = \frac{U_0^{3/2} Q^{1/4}}{g'^{1/2} W_o^{3/4}} \tag{1}$$

where U_0 is river velocity at the mouth (variable in a tidal cycle), Q is river discharge, g' is the reduced gravity (based on density differences between the plume and ocean), and w_e is an entrainment velocity defined to represent the mixing of density and momentum from the lower ocean layer into the upper river plume layer (Hetland, 2010), and has typical values in the range 1–8 mm/s (Kastner et al., 2019; MacDonald & Geyer, 2004). The cross-flow length is determined by the discharge momentum and the alongshore velocity in the surfzone (Jones et al., 2007; Wong et al., 2013)

$$L_a = \frac{U_0^{1/2} Q^{1/2}}{U_{SZ}} \tag{2}$$

where $U_{\rm SZ}$ is a representative value for the wave-driven alongshore currents, usually chosen as the maximum value of wave-driven alongshore currents in the surfzone (Wong et al., 2013). $L_{\rm NF}$ predicts the region in which the momentum of a jet, rather than its buoyancy, controls the flow (Hetland, 2010; Kastner et al., 2019), while L_a can be interpreted as the characteristic length scale for the outflow jet to become bent by the cross-flow (Jones et al., 2007; Wong et al., 2013). The relative magnitude of these two discharge length scales compared to the surfzone width provides a framework to predict the fate of the river water in the coastal system (Kastner et al., 2019; Wong et al., 2013). Kastner et al. (2019) proposed that if $L_{\rm NF} > L_{\rm SZ}$ the river water exits the surfzone as its momentum overcomes the breaking wave forcing. Furthermore, the cross-shore propagation of river water trapped in the surf zone is proportional to $L_{\rm NF}$. Similarly, Wong et al. (2013) proposed that if $L_d/L_{\rm SZ} > 1/10$ the river water is expected to spread across the breaker line as the wave-generated alongshore flow is not strong enough to bend the outflow jet sufficiently close to shore. Conceptually, these models provide a simple way to predict the fate of river discharge in the surfzone that requires data that is typically available or can be readily estimated.

The effects of infragravity (hereafter IG) motions are not considered in the above formulations. Infragravity waves, while small offshore, have been shown to influence the hydrodynamics and morphodynamics of beaches, small tidal inlets and estuaries (Bertin et al., 2019; Bertin & Olabarrieta, 2016; Brocchini, 2020; Elgar et al., 1992; McSweeney et al., 2020; Melito et al., 2020; Mendes et al., 2020; Williams & Stacey, 2016). IG waves result in surface water level fluctuations with periods of 30-300 s that are typically associated with wave groups and result from nonlinear interactions in the incident short waves (Bertin et al., 2018; Henderson et al., 2006; Schäffer, 1993). These waves are strongest near the shoreline (Elgar et al., 1992; Guza & Thornton, 1985), and are observed to propagate upstream in bar-built estuaries (e.g., Williams & Stacey, 2016). Typically these estuaries have shallow and dynamic (sometimes closing) inlets that may block IG energy by bathymetry, where the elevation of the inlet bed is above the tidal low water level in the nearshore (e.g., Williams & Stacey, 2016) or by supercritical ebbing currents (e.g., Dodet et al., 2013). Williams and Stacey (2016) reported field measurements in a small bar-built estuary in Northern California that showed large velocity oscillations within the estuary basin associated with IG motions in the nearshore. Similarly, Bertin et al. (2019) reported high currents during the passage of IG waves crests at a shallow tidal inlet, which resulted in an increase of the sand flux by at least two orders of magnitude that favored inlet closure. IG wave frequencies and amplitudes have been linked to variability in estuary entrance morphologies and offshore wave conditions (e.g., McSweeney et al., 2020; Williams & Stacey, 2016).

The importance of the IG wave forcing has been established primarily as these waves propagate inside small estuaries and inlets influencing estuarine hydrodynamics and the movement of sediment (Bertin et al., 2018, 2019; Brocchini, 2020; Williams & Stacey, 2016), but have not been reported as a factor in the dynamics of small river plumes. In this work we show the first measurements of salinity in the near-field of a small river plume being modulated in the IG wave frequency band, and that the plume itself is steered back and forth as a result of IG wave dynamics in the surfzone. Implications for conceptual models aiming to predict the fate of river water, such as those presented above, are discussed in light of these findings.

FLORES ET AL. 2 of 12



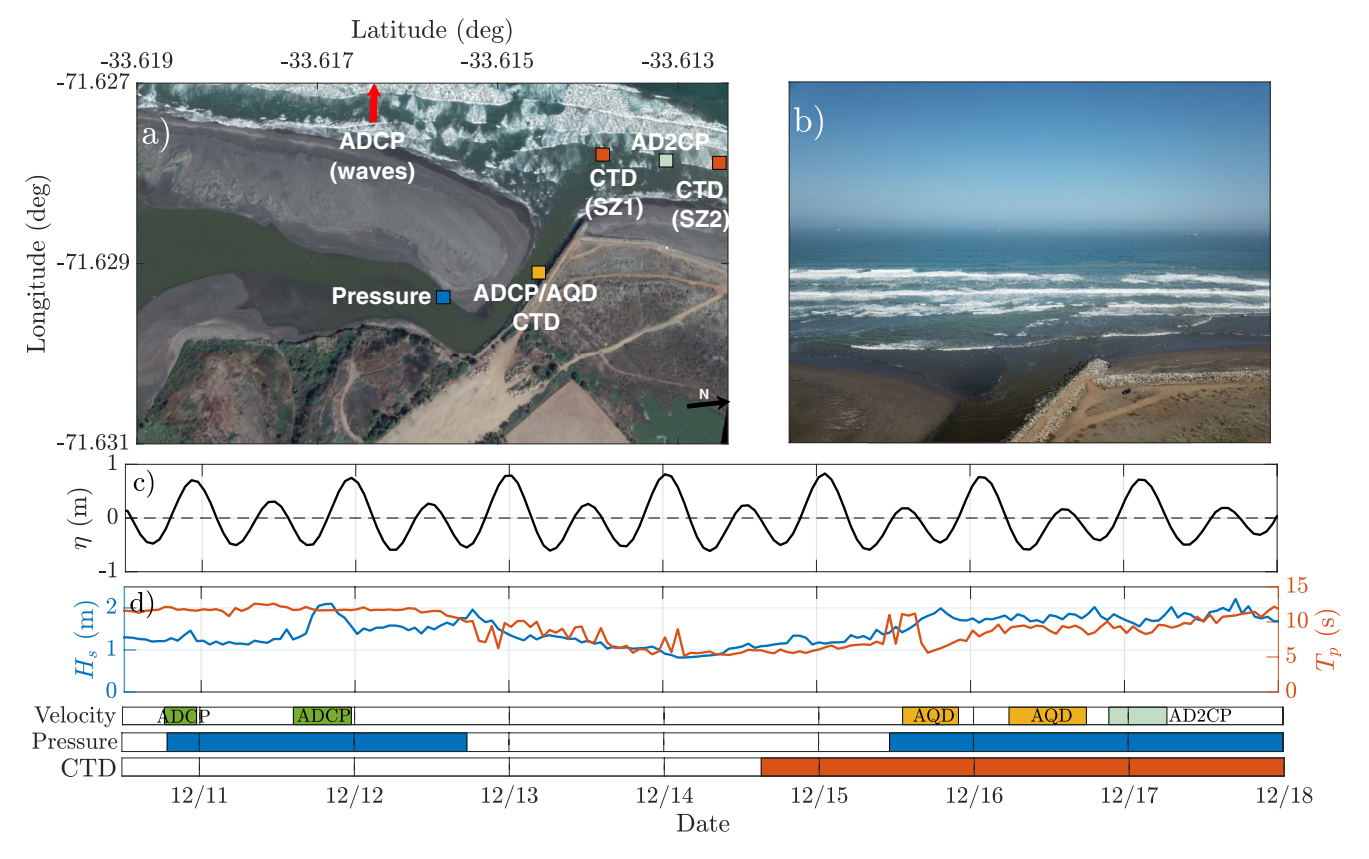


Figure 1. Study area, instrumentation and external forcing. (a) Study area and location of instruments. (b) Drone image of the study area. (c) Tidal elevation at the Port of San Antonio (2 km north from the river mouth). (d) Offshore wave height (blue line) and peak wave period (red line). Colored bars at the bottom of the figure indicate measurement times of the different instruments. For velocity: Acoustic Doppler Current Profiler (ADCP) in outflow channel (green), Aquadopp (AQD) in outflow channel (yellow) and AD2CP in the surfzone (light green). Pressure: RBR fast sampling pressure sensor in the inlet (blue). CTD: Channel and surfzone salinity (red)

2. Field Campaign and Data Analysis

The river plume study was conducted at mouth of the Maipo River, located in Central Chile (Figures 1a and 1b). The Maipo River is a glacial-fed river with headwaters in the Andes and a watershed containing Santiago (Chile's capital and largest city) and other highly urbanized and agricultural areas. As a consequence, there is a growing concern that the river may contain significant amounts of pollutants and fertilizers (Cai et al., 2006; Rosegrant et al., 2000). Planned construction of an external mega-port next to the inlet further motivates the selection of the study site. The Maipo River system drains a 15,000 km² watershed, with an annual average flow rate of approximately 50 m³/s near the river mouth during the past decade. The river discharge is sharply seasonal following rainfall events in the winter and snowpack melting during the spring-summer time (Peña-Guerrero et al., 2020). The coast along the Maipo mouth is exposed to high wave activity, with an annual-mean offshore wave height and peak periods of about 1.5 m and 12 s, respectively (Beyá et al., 2017). Similar to many other coastal regions in Mediterranean climates, the combination of seasonal river flows and strong wave activity results in the formation of a large littoral sandbar at the river mouth, forming a small bar-built estuary that discharges directly into an energetic surfzone, though armoring of the northern edge of the inlet through a substantial jetty prevents northward migration of the inlet (Figures 1a and 1b). Tides in the Maipo region have maximum amplitudes of approximately 1.5 m (e.g., Figure 1c). Overall, the Maipo is both a representative Andean system and one of high importance among Chilean watersheds.

A field campaign was conducted from 10 to 19 December 2019, which coincided with spring tide and low river discharge conditions. Flow rate at the closest gaging station (Cabimbao, BNA 05748001–7, 20 km upstream) indicated that the freshwater river discharge ranged between 5 and 10 m³/s during the campaign (not shown), which was lower than the historical seasonal average and likely attributable to the ongoing mega-drought central

FLORES ET AL. 3 of 12



Chile has experienced since 2010 (Garreaud et al., 2017). A dike that regulated the river was built approximately 3.5 km upstream of the river mouth by the local water company shortly before the field campaign, in order to limit salt intrusion to potable water intakes. Our estimates of inlet discharge used in length scale calculations are based on measurements of velocity profiles in the outflow channel, which were depth averaged, and the assumption of a parabolic cross-section (Figure 1a), rather than on data from the gaging station because of uncertainty in the restriction of flow by this dike. Instruments were deployed at different times during the field campaign, based on their availability and sampling strategies. The measurement periods of the instruments are shown in Figure 1. Conductivity-temperature-depth (CTD) sensors measuring every 15 s were deployed in pairs (surface and bottom) in the center of the outflow channel and in two locations within the surfzone (SZ1 and SZ2, respectively). The SZ1 sensors were deployed directly offshore of the river mouth and in the trajectory of the outflow jet, and the SZ2 sensors were deployed approximately 100 m to the north in the surfzone (Figure 1a). Salinity and water column stratification was determined from the CTD sensors. A pressure sensor sampling at 16 Hz was placed at the bend of the channel (Figure 1) to measure water level in the inlet, capturing tidal and wave components.

Flow velocity in the outflow channel was measured using a new experimental platform, *La Tagua Veloz* (LTV), which consisted of two surfboards joined and a structure that supported a down-looking Acoustic Doppler Current Profiler (ADCP) that extended into the water in the center of the boards (Figure 1a). The LTV was anchored to the bottom of the channel, and redeployed each day. From 10 to 12 December, we used a down-looking ADCP (RDI Workhorse 1200 kHz) sampling at 2 Hz with a vertical resolution of 0.5 m. The shallowness of the outflow channel resulted in only 1–3 useable velocity bins depending on the tidal stage. From 14 December to the end of the campaign, flow velocities in the channel were measured using a Nortek Aquadopp (AQD) mounted to the bottom of the LTV, though instrument errors resulted in useable data only for 15–16 December. The AQD sampled continuously at 2 Hz with 20 cm vertical resolution. The velocity measurements from the RDI ADCP were smoothed using a 10 s moving average, while those from the AQD were averaged in 10 min bursts to obtain mean velocity profiles. A Nortek Signature AD2CP was deployed in the surfzone on 16 December, measuring at 1 Hz for 120 s (every 10 min) for the mean velocities, and on 17 min busts (every hour) at 4 Hz for turbulence measurements (Figure 1a). Unfortunately, this instrument was nearly buried due to sediment movement and had to be recovered after one tidal cycle.

After 12 December, the RDI 1200 kHz ADCP was re-deployed outside of the surfzone in approximately 13 m of water in order to measure the incoming directional wave spectra, from which significant wave height, peak period and peak direction were obtained. The field site is located 2 km south of the Port of San Antonio (Chile's largest port), which maintains an ADCP that measures spectral wave parameters and tidal currents at a location in 20 m of water. Excellent agreement between wave parameters measured by our ADCP and that of the Port of San Antonio (Figure S1 in Supporting Information S1) allowed us to extend our wave time series to the beginning of the campaign when no offshore measurements were available.

Surface salinity energy density spectra were computed based on Fast Fourier Transforms and Parzen lag windows, which resulted in spectra with 20 equivalent degrees of freedom and spectral resolution of 10^{-4} Hz. A continuous wavelet transform using a Morse wavelet was applied to the high frequency pressure data subsampled to 0.25 Hz located inside the channel (Figure 2a). Infragravity velocities and pressure in the inlet were calculated by filtering these frequencies. A 10 s moving average was applied to the downward facing ADCP to smooth the data. To calculate IG velocities, only the first bin was used, corresponding to 81 cm below the instrument, as this was the only cell with consistent data. For both velocity and pressure data, the signals were then bandpass filtered (between the IG periods of 1/30 and 1/300 Hz). A moving variance of these signals using a 10 min window (twice the larger IG period) was used to calculate the magnitude of IG signals in velocity (Figure 2d) and pressure (Figure 2e). Significant IG wave height ($H_{m0,IG}$) was computed as $H_{m0,IG} = 4\sigma$, where σ is the standard deviation of the IG band pass filtered pressure series.

Drone imagery of the outflow channel, the near-field plume and surfzone were acquired using a DJI Mavic Pro quadcopter, equipped with a 4k video camera (e.g., Figure 1b). A total of 25 flights were made spanning a wide range of tide and wave conditions. Most flights were conducted on ebb tide in order to capture the outflow plume as it entered the surfzone. Video rectification was made following the methods outlined in Holman et al. (2017) and using 5–8 ground control points placed on the sand bar and on the northern side of the outflow channel. Cross-shore and alongshore timestacks were constructed from the rectified video frames. RGB images showing turbid (sediment laden) plume waters were transformed into a "Hue-Saturation-Value" (HSV) color space (e.g.,

FLORES ET AL. 4 of 12

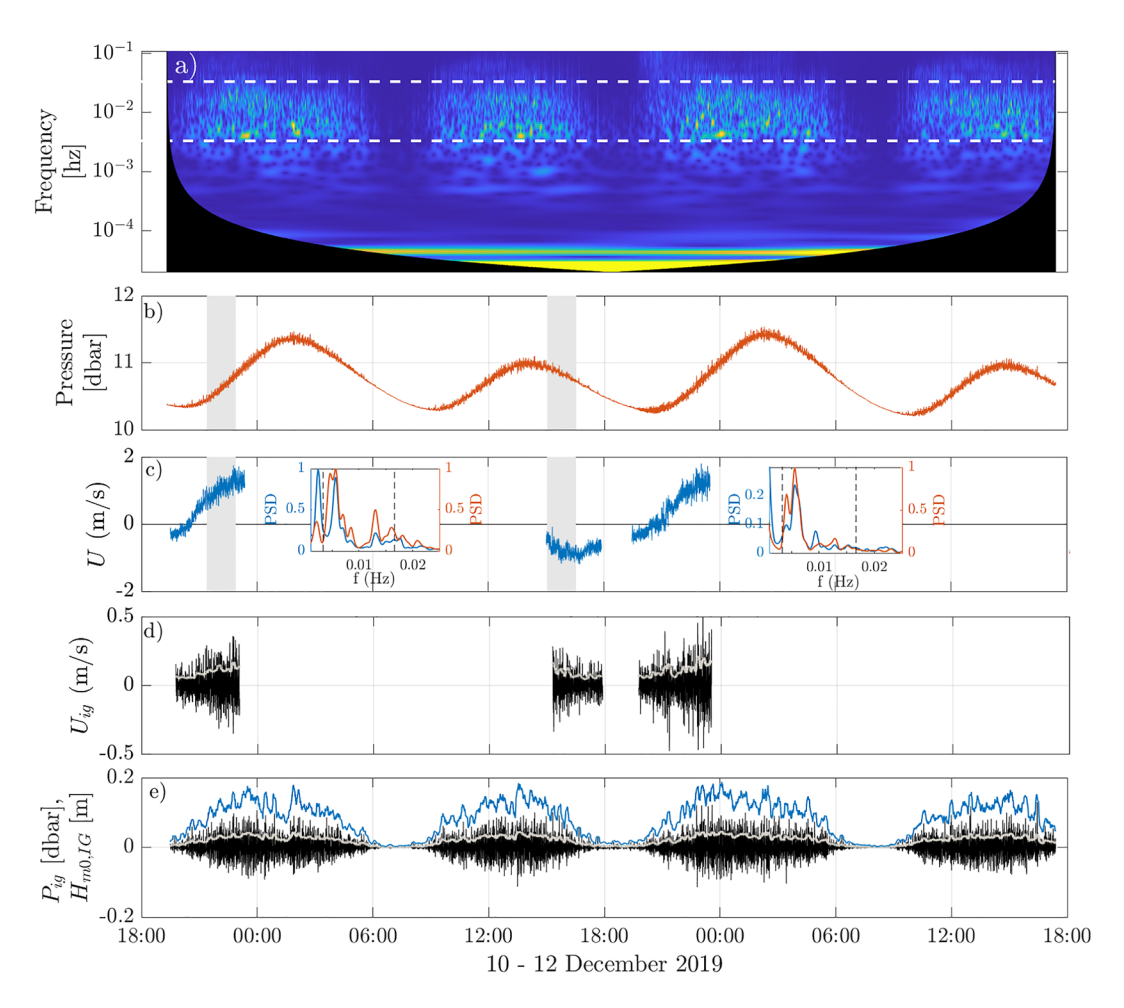


Figure 2. Inlet dynamics. (a) Inlet pressure wavelet spectrum. Blue and yellow colors represent low and high energy regions, respectively. White dashed lines indicate the infragravity (IG) frequency band (30–300 s). (b) Raw pressure (16 Hz). (c) Surface along channel Acoustic Doppler Current Profiler (ADCP) velocity (first bin of ADCP). The insets correspond to pressure spectra (red lines) and channel velocity spectra (blue lines). The inset on the left corresponds to spectra computed for a time period indicated by the first gray shaded area in panels b and c, and the inset on the right corresponds to spectra computed for a time period indicated by the second gray shaded area in panels b and c. (d) Velocity signal associated to the IG band (black line), corresponding to a 1/30-1/300 s bandpass filter surface along channel velocity, and 10 min moving variance of the bandpass filtered signal (gray). (e) Pressure signal associated to the IG band (black line), corresponding to a 1/30-1/300 s bandpass filter of the pressure data, a 10 min moving variance of the bandpass filtered signal (gray line), and IG wave height $H_{m0,IG}$ (blue line).

Aarninkhof et al., 2003) in order to mask the signature of breaking waves, enhance contrast between plume and ocean waters and finally extract the plume edge using a pixel threshold algorithm. An example is shown in Figure S2 of Supporting Information S1.

3. Observations and Results

Offshore wave conditions showed variability during the measurement campaign, with significant wave heights between 1 and 2 m and peak wave periods in the range of 8–12 s (Figure 1d). Maximum and minimum tidal range was 1.35 and 0.50 m, respectively (Figure 1c). The channel velocity and inlet pressure signals are shown in Figure 2 for three tidal cycles at the beginning of the campaign (10 – 12 December), where plotted velocities are the first velocity bin of the downward-facing instrument. The along channel velocity switches sign with the tides, with landward (positive) flow during the flood and oceanward (negative) flow during ebb (Figures 2c and 2d). Outflow velocities during ebb tide reach a maximum of 1 m/s, while the inflow velocities during the flood have maximum values close to 1.5 m/s (Figure 2c).

FLORES ET AL. 5 of 12

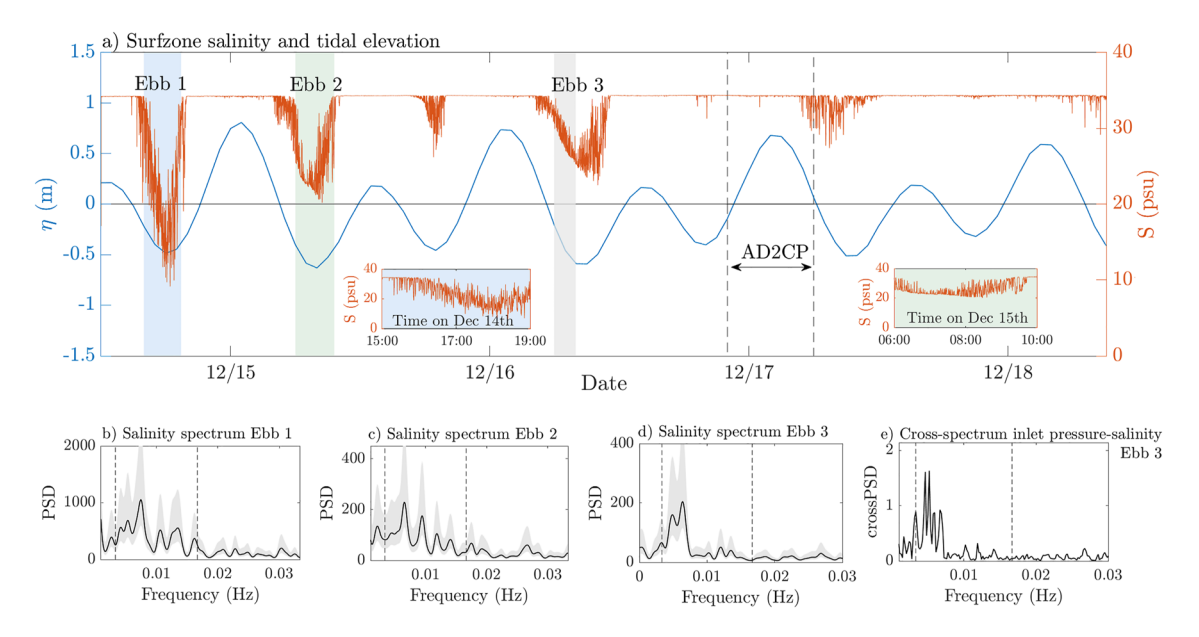


Figure 3. Surfzone salinity. (a) Surfzone salinity (red line) and tidal elevation (blue line). Insets show a zoomed time period corresponding to the light blue and light green shaded areas. The gray area indicates the time period for which the cross-spectrum between surfzone salinity and inlet pressure is computed (shown in panel e). Vertical dashed lines indicate the measurement period of the AD2CP (see SI). (c–e) Salinity power spectrum for Ebb1, Ebb2 and Ebb3 as indicated in panel (a). Gray areas indicate a 95% confidence interval. (e) Surfzone salinity and inlet pressure cross-spectrum, computed for a time period indicated by the gray shaded area in panel (a).

The inlet pressure data shows oscillating motions on top of the tidally-induced water surface elevation (Figure 2b). These oscillations are modulated by the tide; they are present primarily during the flood and cease as the ebb flow strengthens (Figures 2a,2b and 2e). The wavelet analysis of the pressure data confirms that these oscillations are associated with IG motions in the nearshore, as most part of the spectral energy is contained in the IG wave band and with a temporal evolution that is consistent with the tidal modulation (Figures 2a and 2b). The velocity oscillations associated with the IG wave forcing are strong during both phases of the tide, reaching up to 25 cm/s during the flood and 50 cm/s during the early ebb (Figure 2d). Significant IG wave heights (H_{m0}) reach maximum values of approximately 20 cm during flood tides (Figure 2e). Large H_{m0} values (15–18 cm) are observed during early ebb tides, which progressively decrease as the ebb flow intensifies (Figure 2c and 2e). Spectra of inlet pressure and channel velocity for both flood and ebb tides are very similar; most of the energy is contained within the IG band and with the same peak frequencies (see insets in Figure 2c).

Surfzone salinity from the SZ1 mooring shows that freshwater comes out of the estuary only during ebb tides (Figure 3a). Once the flood tide starts and flow reversal occurs, the freshwater outflow rapidly ceases and surfzone salinity increases to ocean values (Figure 3a). The surfzone salinity signal presents high variability during the study period, with values as low as 10 psu but typically on the order of 25 psu (Figure 3a). Persistent low frequency oscillations in salinity are observed during ebb tides when there is freshwater leaving the estuary (see insets in Figure 3a). Spectral analysis of the surfzone salinity data confirms that these oscillations occur at the IG wave frequencies (Figures 3b–3d). Figures 3b–3d show the salinity spectrum for three ebb tide periods (indicated in panel (a)); in all of these spectra the majority of energy is contained in the IG wave band. Peak spectral periods are in the range of 2–4 min, typical of IG wave forcing in the nearshore. Figure 3e shows the cross-spectrum between inlet pressure and surfzone salinity for the time period corresponding to the gray shaded area in Figure 3a. The cross-spectrum shows that these signals are strongly correlated in the IG band, and with peak frequencies that coincide with the peak frequencies observed in the salinity spectrum shown in Figure 3d.

Surfzone velocities measured by the Nortek Signature AD2CP on 16–17 December show a persistent northwest-ward flow during the flood, with a northward (alongshore) component of 25–30 cm/s and westward (offshore) velocities of similar magnitude (Figure S3a in Supporting Information S1). Mean velocity spectra estimated from five 17 min data bursts at 4 Hz indicates that the surfzone velocities are modulated primarily at IG wave frequencies, with peak periods in the 30 s-2 min band (Figure S3b in Supporting Information S1).

FLORES ET AL. 6 of 12

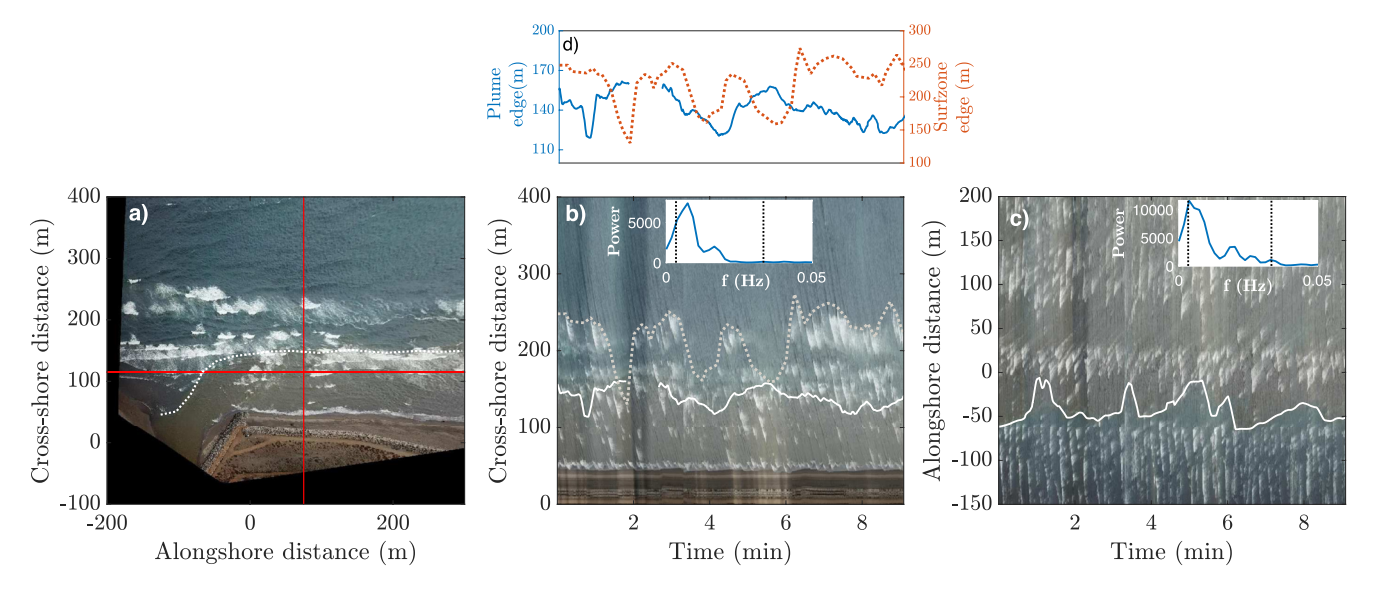


Figure 4. Drone plume and surfzone observations. (a) Example of rectified drone image on 14 Dec. Red lines represent the cross-shore and alongshore coordinates for which the cross-shore and alongshore timestacks shown in panels (b and c) are extracted. The dotted white line represents the plume edge, for which time variations are shown in panels (b and c). (b) Cross-shore timestack. (c) Alongshore timestack. In all panels, the white line shows the plume edge. The gray dotted line in panel (b) indicates the edge of the surfzone. The insets in panels (b and c) correspond to the spectrum of the time series of plume edge position (t and y). Vertical dashed lines indicate the infragravity frequency band. (d) Time series of cross-shore plume edge (blue line, same as white line in (b)) and surfzone edge (red line, same as gray dotted line in (b)) for the time period shown in the drone images.

We use drone videos and images to visualize and quantify the response of the combined inlet and plume region to the IG wave forcing (Figure 4). Images are shown only for 14 December, as the river outflow was turbid enough to create sufficient color contrast between the plume and ocean waters following a breach of the dike. The drone imaging shows that the plume bends shortly after exiting the estuary and flows parallel to the coast, and that it is effectively trapped and confined to the coast, as discussed below (Figures 4a and 4b). We also observe that the plume is modulated at the IG wave periods in the along- and across-shore directions (Figures 4b and 4c). Using turbidity as a proxy for river water, Figures 4a and 4b clearly show that the river outflow is unable to extend further offshore than the shallowest breaker line. The timestacks show that the plume edge (white line) oscillates back and forth in the across-shore and alongshore directions, with periods of 2–3 min and ranges of 20–50 m (Figures 4b and 4c). Moreover, the spectra of the time series of plume edge position show that a large fraction of the total spectral energy is contained in the IG band, with a peak frequency of approximately 0.004 Hz (period of 4 min, see insets in Figures 4b and 4c).

The structure and width of the surfzone can also be inferred from wave breaking visible in Figure 4b and the time series of surfzone edge position in Figure 4d. The surfzone consists of an inshore and an offshore break, which are centered approximately 150 and 200 m seaward of the high water mark, respectively. The strength of breaking varies during the 9 min timestack in Figure 4b; breaking ceases at the offshore break at the 2, 4 and 6 min marks, suggesting variability in surfzone at IG timescales (Figure 4d). The spectrum of surfzone edge position (Figure 4c) has a peak frequency of 0.008 Hz (~125 s, not shown).

4. Discussion

The influence of IG wave forcing is felt throughout the Maipo inlet and plume system, as evidenced by variations at IG wave frequencies in salinity, velocity and pressure measurements in the inlet, discharge channel and the near-field plume region (Figures 2 and 3). This conclusion is further supported by drone imaging, which documents large-scale movement of the plume boundary at IG wave frequencies (Figure 4).

An important question that arises from the observed inlet-plume dynamics is whether the observed modulations at IG frequencies result directly from IG waves (with a water level signal) or are related to modulations in the wave-induced currents by wave groups. The spectra and cross-spectra shown in Figures 2 and 3 strongly suggest that the observed modulations at IG frequencies in velocity and surfzone salinity result primarily from IG

FLORES ET AL. 7 of 12



waves, as both these signals are highly coherent with pressure (water levels) and oscillate at the same frequencies (Figures 2c and 3e). It is also possible that modulation of wave-induced currents related to wave groups plays a role in setting up IG modulations, but it is not possible to fully evaluate the role of this generation process with our data set.

Our observations show that the plume was confined to the surfzone (e.g., Figure 4a). Modeling studies (both realistic and idealized) have evaluated momentum balances in low discharge rivers and tidal inlets showing that gradients in momentum fluxes associated with incoming breaking waves slow the outgoing plume, preventing it from expanding seaward (e.g., Feddersen et al., 2016; Moghimi et al., 2019; Rodriguez et al., 2018). The breaking of short waves exerts a depth-integrated wave force that limits the cross-shore spreading of the plume and traps freshwater in the surfzone (e.g., Moghimi et al., 2019; Rodriguez et al., 2018). The wave force may have an along-shore component due to obliquely incident waves or bathymetric effects, which can generate alongshore flows (e.g., Longuet-Higgins, 1970) and alongshore transport of freshwater (e.g., Feddersen et al., 2016). Our offshore wave measurements indicate that wave height and direction were 1 m and 30°, respectively, for the case shown in Figure 4, which are within ranges observed to generate alongshore flows and trapping in previous studies (e.g., Feddersen et al., 2016; Moghimi et al., 2019). In the following discussion we investigate the mechanisms by which the IG forcing may modify the trajectory and width of the plume.

We describe the trajectory and fate of freshwater in the surfzone in terms of the length scales defined in Section 1, L_a , $L_{\rm NF}$ and $L_{\rm SZ}$. Since surfzone velocities were not measured during the entire study, we developed estimates for the alongshore currents based on a simple SWAN model (Booij et al., 1999) that was forced with wave statistics measured by the offshore ADCP and bathymetry derived from drone imaging using the cBathy algorithm (Holman et al., 2013). The alongshore currents were calculated from a simplified alongshore momentum balance that included the modeled wave-induced force from SWAN and bottom friction in the form of a quadratic drag law (e.g., Feddersen et al., 1998). SWAN dissipation fields agreed well with the spatial distribution of wave breaking observed in timex images, providing qualitative validation of the SWAN model (Figure S4 in Supporting Information S1). River outflow momentum was estimated from velocity measurements in the channel (e.g., Figure 2c). Estimates of L_a and $L_{\rm SZ}$ for the Maipo site range between 10–20 and 100–300 m (e.g., Figures 4b and 4c), respectively, resulting in $L_a/L_{\rm SZ}$ in the range of 0.01–0.09. Thus, $L_a/L_{\rm SZ}$ values are below and up to the threshold of 0.1 proposed by Wong et al. (2013), suggesting that the outflow will be trapped in the surfzone. Figure 4a is consistent with this scaling, as it clearly shows that the outflow is bent shortly after exiting the river mouth.

On the other hand, estimates of $L_{\rm NF}$ range from 20 to 300 m during our study period, resulting in $L_{\rm NF}/L_{\rm SZ}$ in the range of 0.2–2.5. Thus, there are a few cases where $L_{\rm NF} > L_{\rm SZ}$ and the conceptual model based on $L_{\rm NF}$ predicts that the discharge momentum is sufficient for river water to escape the surfzone. For these cases, we find that $L_a/L_{\rm SZ} < 1/10$, suggesting that even though the river had enough momentum to escape the surfzone, the influence of alongshore currents inhibited that process. Our scaling results and drone observations (e.g., Figure 4) are in good agreement with the framework proposed in Wong et al. (2013) and Kastner et al. (2019); the plume is completely trapped by the wave forcing and cannot spread beyond the shallowest breaker line. Additional drone imaging (Figure S5 in Supporting Information S1) confirms that this was always the case during our study period. We note that river discharge was low during our observational period; satellite images from other periods confirm that the river discharge can penetrate through the surfzone during high discharge conditions (not shown).

The length scales defined in Section 1 can be influenced by the IG wave forcing, suggesting temporal changes in the dominant balance that determines the fate of river water. In the Maipo, river velocity, and thus river momentum, show fluctuations due to IG wave forcing on the order of 15–20 cm/s, which is equivalent to 15%–20% of peak ebb velocity in the channel (Figures 2c and 2d). Noting that $L_{NF} \sim U_0^{7/4}$ (Equation 1), a 20% change in U_0 would result in approximately a 40% change in L_{NF} induced by the IG waves. Kastner et al. (2019) found that maximum drifter excursion in the surfzone scales linearly with L_{NF} ; thus, river velocity fluctuations induced by IG waves may be responsible for the observed modulation in the cross-shore extent of plume water. Based on our estimates of L_{NF} , the IG band fluctuations in channel velocity are predicted to result in a 5–120 m fluctuation in the cross-shore excursion of the river water into the surf zone, roughly consistent with the 20–50 m modulations of the plume edge observed in Figure 4b and 4d. Considering that the average plume width is approximately 90 m (the average position of the offshore edge of the plume is x = 140 m, Figure 4b), these fluctuations modify the plume width by 20%–50%. The IG influence on L_a is harder to estimate because it scales with the ratio U_0/U_{SZ} .

FLORES ET AL. 8 of 12

a) Low wave amplitude

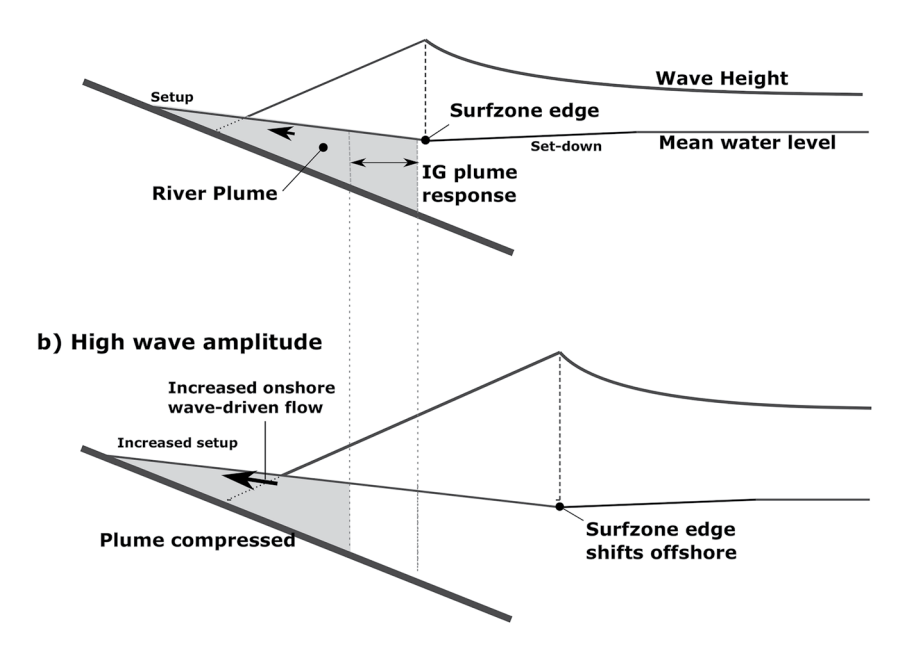


Figure 5. Schematic of the proposed mechanism of plume width modulation at infragravity (IG) timescales. (a) Low wave conditions. The plume is able to extend offshore due to reduced wave breaking and wave-driven onshore flow (b) High wave conditions. The plume compresses due to enhanced wave-driven onshore flow at the surface. The arrows indicate the strength of the onshore wave-driven currents. Schematic elements of the surfzone response to IG waves are based on the schematic from (Symonds et al., 1982).

Both U_0 and $U_{\rm SZ}$ are expected to vary due to IG wave forcing, but the IG band variation in $U_{\rm SZ}$ cannot be estimated from our measurements. The observed IG band variations in river velocity appear to be of sufficient magnitude to influence plume trapping and the penetration of the plume into the surfzone.

We noted in Section 3 that the intensity of breaking at the offshore breaker varied at IG frequencies. This suggests that L_{SZ} also increases and decreases at IG frequencies. It is apparent in Figure 4b and 4d that periods of reduced offshore breaking, and thus smaller L_{SZ} , usually correspond to periods when the plume width is larger, and viceversa. Correlation analysis indicates that the plume edge and surfzone width shown in Figure 4d are negatively correlated, with a correlation coefficient of approximately -0.25 (p-value < 0.05). Thus, modifications in surfzone width and the strength of surfzone circulation may also influence the plume width; the plume expands and contracts as the surfzone contracts and expands. Modulations in surfzone width result from the arrival and depth-limited breaking of lower and higher amplitude waves, that is, wave groups (Apotsos et al., 2007; Flores et al., 2016; Lentz & Raubenheimer, 1999; O'Connor et al., 1999; Svendsen, 1984). Wave-driven cross-shore currents in the surfzone generate a Lagrangian overturning circulation cell with onshore flow at the surface resulting from the onshore-directed Eulerian flow driven by wave breaking and the Stokes drift (e.g., Kumar et al., 2012; Pezerat et al., 2022; Zheng et al., 2017). We hypothesize that stronger onshore flow at the surface associated with large amplitude waves (e.g., Guérin et al., 2018; Svendsen, 1984) transports freshwater toward the coast and compresses the river plume, and that weaker onshore flow during periods of low amplitude waves enables the plume to expand offshore. During times with lower amplitude waves the breaker line is also closer to shore; since the plume is wider it approaches the breaker line in this phase of the oscillation. From Figure 4b and 4d, we estimate that the average onshore velocity required to displace the plume edge approximately 35 m between minutes 5.5-8 is 25 cm/s. This estimate is consistent with the magnitude of surface flow velocities reported in modeling (e.g., Kumar et al., 2012; Pezerat et al., 2022; Zheng et al., 2017) and field (e.g., Faria et al., 1998; Faria et al., 2000) surfzone circulation studies. A schematic of the proposed mechanism is shown in Figure 5. This mechanism is consistent with the generation of IG forcing by a time-varying breakpoint resulting from wave groups breaking closer and farther from the shore (Contardo & Symonds, 2013; Symonds et al., 1982). In the Maipo, a time-varying breakpoint (e.g., Figure 4b) is likely to be the more effective mechanism of IG wave generation due to a steep bottom slope (\sim 0.01) and wave group periods of \sim 180 – 240 s (e.g., Battjes et al., 2004;

FLORES ET AL. 9 of 12



Pomeroy et al., 2012). We note that although this mechanism is plausible based on our data set, further work needs to be done to evaluate its occurrence over a wide range of wave conditions. Finally, increased wave-setup during periods of large amplitude waves (e.g., Apotsos et al., 2007; Svendsen, 1984) may influence the pressure gradient at the mouth (e.g., Rodriguez et al., 2018), reducing flow from the river channel and thus contributing to a narrower plume based on a reduction in $L_{\rm NF}$ as described above. Thus, IG modulation of the surfzone results in a decrease in $L_{\rm NF}$ when $L_{\rm SZ}$ is large and vice versa, resulting in a plume that expands and contracts at IG frequencies.

In addition to influencing discharge pathways by steering and modulating the outflow plume, we expect that the IG wave forcing contributes to mixing and dilution of the river water in the surfzone. In the conceptual model shown in Figure 5, the surfzone edge and plume edge alternately move onshore and offshore with IG band modulation. At the plume edge, horizontal density gradients are high and repeated compression and expansion of the plume likely also generates vertical stratification through straining. At the edge of the surfzone, wave breaking is strong, resulting in high turbulence levels. The IG modulation of the system repeatedly moves these two boundaries cross-shore, substantially expanding the area over which mixing occurs.

5. Summary

Using field observations we show the first measurements of nearshore IG motions modulating the dynamics of a small river plume in the surfzone. We observe that outflow velocity, wave breaking intensity and plume salinity signal all vary in the IG frequency band, and that the river plume also expands and contracts at these frequencies. Scaling analysis suggests that variability in the inlet discharge and surfzone currents may also contribute to plume forcing at IG frequencies. This work suggests that IG waves in the nearshore may be important in regulating the fate and transport of freshwater and river-borne materials in small coastal river systems along wave dominated coasts.

Data Availability Statement

Open Research Data from the paper are available at https://doi.org/10.5281/zenodo.5762101.

Acknowledgments

This work was funded by ANID-Chile through FONDECYT grant 11190378 (RPF). RPF also acknowledges support from FONDECYT grant 1190805, and from Departamento de Obras Civiles at Universidad Técnica Federico Santa María. MEW was supported by FOND-ECYT 11191077. Raúl P. Flores and Megan E. Williams acknowledge support from ANID-Chile through FONDAP 15110017 (CIGIDEN). The authors acknowledge support from NSF OCE-1923941 Project. The authors would like to thank Ignacio Jainaga for work on drone imaging and assistance with fieldwork: Randy Finke and ECIM (Estación Costera de Investigaciones Marinas) for installing the offshore ADCP; Sarah Giddings, Patricio Catalán and Rodrigo Cienfuegos for lending instruments; Melissa Moulton, Chris Chickadel and Iim Thomson for valuable discussions on surfzone and IG wave dynamics.

References

- Aarninkhof, S. G., Turner, I. L., Dronkers, T. D., Caljouw, M., & Nipius, L. (2003). A video-based technique for mapping intertidal beach bathymetry. *Coastal Engineering*, 49(4), 275–289. https://doi.org/10.1016/s0378-3839(03)00064-4
- Apotsos, A., Raubenheimer, B., Elgar, S., Guza, R., & Smith, J. A. (2007). Effects of wave rollers and bottom stress on wave setup. *Journal of Geophysical Research*, 112(C2), C02003. https://doi.org/10.1029/2006jc003549
- Basdurak, N., Largier, J., & Nidzieko, N. (2020). Modeling the dynamics of small-scale river and creek plumes in tidal waters. *Journal of Geophysical Research: Oceans*, 125(7), e2019JC015737. https://doi.org/10.1029/2019jc015737
- Battjes, J., Bakkenes, H., Janssen, T., & van Dongeren, A. R. (2004). Shoaling of subharmonic gravity waves. *Journal of Geophysical Research*, 109, C02009. https://doi.org/10.1029/2003jc001863
- Bertin, X., De Bakker, A., Van Dongeren, A., Coco, G., André, G., Ardhuin, F., et al. (2018). Infragravity waves: From driving mechanisms to impacts. *Earth-Science Reviews*, 177, 774–799. https://doi.org/10.1016/j.earscirev.2018.01.002
- Bertin, X., Mendes, D., Martins, K., Fortunato, A. B., & Lavaud, L. (2019). The closure of a shallow tidal inlet promoted by infragravity waves. Geophysical Research Letters, 46(12), 6804–6810. https://doi.org/10.1029/2019gl083527
- Bertin, X., & Olabarrieta, M. (2016). Relevance of infragravity waves in a wave-dominated inlet. *Journal of Geophysical Research: Oceans*, 121, 5418–5435. https://doi.org/10.1002/2015jc011444
- Beyá, J., Álvarez, M., Gallardo, A., Hidalgo, H., & Winckler, P. (2017). Generation and validation of the chilean wave atlas database. *Ocean*
- Modelling, 116, 16–32. https://doi.org/10.1016/j.ocemod.2017.06.004
 Booij, N., Ris, R. C., & Holthuijsen, L. H. (1999). A third-generation wave model for coastal regions: 1. Model description and validation. Journal
- Brocchini, M. (2020). Wave-forced dynamics in the nearshore river mouths, and swash zones. Earth Surface Processes and Landforms, 45(1), 75–95. https://doi.org/10.1002/esp.4699
- Cai, X., Ringler, C., & Rosegrant, M. W. (2006). In Modeling water resources management at the basin level: Methodology and application to the Maipo River basin (Vol. 149). Intl Food Policy Res Inst.
- Contardo, S., & Symonds, G. (2013). Infragravity response to variable wave forcing in the nearshore. *Journal of Geophysical Research: Oceans*, 118, 7095–7106. https://doi.org/10.1002/2013jc009430
- Delpey, M., Ardhuin, F., Otheguy, P., & Jouon, A. (2014). Effects of waves on coastal water dispersion in a small estuarine bay. *Journal of Geophysical Research: Oceans*, 119, 70–86. https://doi.org/10.1002/2013jc009466
- Dodet, G., Bertin, X., Bruneau, N., Fortunato, A. B., Nahon, A., & Roland, A. (2013). Wave-current interactions in a wave-dominated tidal inlet. Journal of Geophysical Research: Oceans, 118, 1587–1605. https://doi.org/10.1002/jgrc.20146
- Elgar, S., Herbers, T., Okihiro, M., Oltman-Shay, J., & Guza, R. (1992). Observations of infragravity waves. *Journal of Geophysical Research*, 97(C10), 15573–15577. https://doi.org/10.1029/92jc01316

FLORES ET AL. 10 of 12

of Geophysical Research, 104(C4), 7649-7666. https://doi.org/10.1029/98jc02622



- Faria, A. G., Thornton, E., Lippmann, T., & Stanton, T. (2000). Undertow over a barred beach. *Journal of Geophysical Research*, 105(C7), 16999–17010. https://doi.org/10.1029/2000jc900084
- Faria, A. G., Thornton, E., Stanton, T., Soares, C. k., & Lippmann, T. (1998). Vertical profiles of longshore currents and related bed shear stress and bottom roughness. *Journal of Geophysical Research*, 103(C2), 3217–3232. https://doi.org/10.1029/97jc02265
- Feddersen, F. (2012). Scaling surf zone turbulence. Geophysical Research Letters, 39(18), L18613. https://doi.org/10.1029/2012g1052970
- Feddersen, F., Guza, R., Elgar, S., & Herbers, T. (1998). Alongshore momentum balances in the nearshore. *Journal of Geophysical Research*, 103(C8), 15667–15676. https://doi.org/10.1029/98jc01270
- Feddersen, F., Olabarrieta, M., Guza, R., Winters, D., Raubenheimer, B., & Elgar, S. (2016). Observations and modeling of a tidal inlet dye tracer plume. *Journal of Geophysical Research: Oceans*, 121, 7819–7844. https://doi.org/10.1002/2016jc011922
- Flores, R. P., Catalán, P. A., & Haller, M. C. (2016). Estimating surfzone wave transformation and wave setup from remote sensing data. *Coastal Engineering*, 114, 244–252. https://doi.org/10.1016/j.coastaleng.2016.04.008
- Garreaud, R. D., Alvarez-Garreton, C., Barichivich, J., Boisier, J. P., Christie, D., Galleguillos, M., et al. (2017). The 2010–2015 megadrought in central Chile: Impacts on regional hydroclimate and vegetation. *Hydrology and Earth System Sciences*, 21(12), 6307–6327. https://doi. org/10.5194/hess-21-6307-2017
- Guérin, T., Bertin, X., Coulombier, T., & de Bakker, A. (2018). Impacts of wave-induced circulation in the surf zone on wave setup. *Ocean Modelling*, 123, 86–97. https://doi.org/10.1016/j.ocemod.2018.01.006
- Guza, R., & B. Thornton, E. (1985). Velocity moments in nearshore. Journal of Waterway, Port, Coastal, and Ocean Engineering, 111(2), 235–256. https://doi.org/10.1061/(asce)0733-950x(1985)111:2(235)
- Henderson, S. M., Guza, R., Elgar, S., Herbers, T., & Bowen, A. (2006). Nonlinear generation and loss of infragravity wave energy. *Journal of Geophysical Research*, 111, C12007. https://doi.org/10.1029/2006jc003539
- Hetland, R. D. (2010). The effects of mixing and spreading on density in near-field river plumes. *Dynamics of Atmospheres and Oceans*, 49(1), 37–53. https://doi.org/10.1016/j.dynatmoce.2008.11.003
- Holman, R., Brodie, K. L., & Spore, N. J. (2017). Surf zone characterization using a small quadcopter: Technical issues and procedures. IEEE Transactions on Geoscience and Remote Sensing, 55(4), 2017–2027. https://doi.org/10.1109/tgrs.2016.2635120
- Holman, R., Plant, N., & Holland, T. (2013). cBathy: A robust algorithm for estimating nearshore bathymetry. *Journal of Geophysical Research: Oceans*, 118, 2595–2609. https://doi.org/10.1002/jgrc.20199
- Izett, J. G., & Fennel, K. (2018). Estimating the cross-shelf export of riverine materials: Part 2. Estimates of global freshwater and nutrient export. Global Biogeochemical Cycles, 32(2), 176–186. https://doi.org/10.1002/2017gb005668
- Jones, G. R., Nash, J. D., Doneker, R. L., & Jirka, G. H. (2007). Buoyant surface discharges into water bodies. I: Flow classification and prediction methodology. *Journal of Hydraulic Engineering*, 133(9), 1010–1020. https://doi.org/10.1061/(asce)0733-9429(2007)133:9(1010)
- Kastner, S., Horner-Devine, A., & Thomson, J. (2019). A conceptual model of a river plume in the surf zone. *Journal of Geophysical Research:*Oceans. 124, 8060–8078. https://doi.org/10.1029/2019ic015510
- Kumar, N., Voulgaris, G., Warner, J. C., & Olabarrieta, M. (2012). Implementation of the vortex force formalism in the coupled ocean-atmosphere-wave-sediment transport (coawst) modeling system for inner shelf and surf zone applications. *Ocean Modelling*, 47, 65–95. https://doi.org/10.1016/j.ocemod.2012.01.003
- Lentz, S., & Raubenheimer, B. (1999). Field observations of wave setup. Journal of Geophysical Research, 104(C11), 25867–25875. https://doi.org/10.1029/1999ic900239
- Longuet-Higgins, M. S. (1970). Longshore currents generated by obliquely incident sea waves: 1. *Journal of Geophysical Research*, 75(33), 6778–6789. https://doi.org/10.1029/ic075j033p06778
- Longuet-Higgins, M. S., & Stewart, R. (1964). Radiation stresses in water waves; a physical discussion, with applications. Deep-Sea Research and Oceanographic Abstracts, 11(4), 529–562. https://doi.org/10.1016/0011-7471(64)90001-4
- MacDonald, D. G., & Geyer, W. R. (2004). Turbulent energy production and entrainment at a highly stratified estuarine front. *Journal of Geophysical Research*, 109, C05004. https://doi.org/10.1029/2003jc002094
- McSweeney, S., Kennedy, D., Rutherfurd, I., & Stout, J. (2017). Intermittently closed/open lakes and lagoons: Their global distribution and boundary conditions. *Geomorphology*, 292, 142–152. https://doi.org/10.1016/j.geomorph.2017.04.022
- McSweeney, S., Stout, J. C., & Kennedy, D. M. (2020). Variability in infragravity wave processes during estuary artificial entrance openings. Earth Surface Processes and Landforms, 45(13), 3414–3428. https://doi.org/10.1002/esp.4974
- Melito, L., Postacchini, M., Sheremet, A., Calantoni, J., Zitti, G., Darvini, G., et al. (2020). Hydrodynamics at a microtidal inlet: Analysis of propagation of the main wave components. *Estuarine, Coastal and Shelf Science*, 235, 106603. https://doi.org/10.1016/j.ecss.2020.106603
- Mendes, D., Fortunato, A. B., Bertin, X., Martins, K., Lavaud, L., Silva, A. N., et al. (2020). Importance of infragravity waves in a wave-dominated inlet under storm conditions. *Continental Shelf Research*. 192, 104026. https://doi.org/10.1016/j.csr.2019.104026
- Milliman, J. D., & Syvitski, J. P. (1992). Geomorphic/tectonic control of sediment discharge to the ocean: The importance of small mountainous rivers. The Journal of Geology, 100(5), 525–544. https://doi.org/10.1086/629606
- Moghimi, S., Özkan-Haller, H. T., Akan, Ç., & Jurisa, J. T. (2019). Mechanistic analysis of the wave-current interaction in the plume region of a partially mixed tidal inlet. *Ocean Modelling*, 134, 110–126. https://doi.org/10.1016/j.ocemod.2018.12.003
- O'Connor, B. A., Pan, S., Nicholson, J., MacDonald, N., & Huntley, D. A. (1999). A 2d model of waves and undertow in the surf zone. *Coastal Engineering*, 1998, 286–296.
- Peña-Guerrero, M. D., Nauditt, A., Muñoz-Robles, C., Ribbe, L., & Meza, F. (2020). Drought impacts on water quality and potential implications for agricultural production in the Maipo River Basin, Central Chile. *Hydrological Sciences Journal*, 65(6), 1005–1021. https://doi.org/10.10
- Pezerat, M., Bertin, X., Martins, K., & Lavaud, L. (2022). Cross-shore distribution of the wave-induced circulation over a dissipative beach under storm wave conditions. *Journal of Geophysical Research: Oceans*, 127, e2021JC018108. https://doi.org/10.1029/2021jc018108
- Pomeroy, A., Lowe, R., Symonds, G., Van Dongeren, A., & Moore, C. (2012). The dynamics of infragravity wave transformation over a fringing reef. *Journal of Geophysical Research*, 117, C11022. https://doi.org/10.1029/2012jc008310
- Rodriguez, A. R., Giddings, S. N., & Kumar, N. (2018). Impacts of nearshore wave-current interaction on transport and mixing of small-scale buoyant plumes. Geophysical Research Letters, 45(16), 8379–8389. https://doi.org/10.1029/2018gl078328
- Rosegrant, M. W., Ringler, C., McKinney, D. C., Cai, X., Keller, A., & Donoso, G. (2000). Integrated economic-hydrologic water modeling at the basin scale: The Maipo River basin. *Agricultural Economics*, 24(1), 33–46. https://doi.org/10.1016/s0169-5150(00)00113-4
- Schäffer, H. A. (1993). Infragravity waves induced by short-wave groups. *Journal of Fluid Mechanics*, 247, 551–588. https://doi.org/10.1017/s0022112093000564
- Stive, M. J., & Wind, H. G. (1982). A study of radiation stress and set-up in the nearshore region. Coastal Engineering, 6(1), 1–25. https://doi.org/10.1016/0378-3839(82)90012-6

FLORES ET AL. 11 of 12



10.1029/2021GL097467



- Svendsen, I. A. (1984). Mass flux and undertow in a surf zone. Coastal Engineering, 8(4), 347–365. https://doi.org/10.1016/0378-3839(84)90030-9 Symonds, G., Huntley, D. A., & Bowen, A. J. (1982). Two-dimensional surf beat: Long wave generation by a time-varying breakpoint. Journal of Geophysical Research, 87(C1), 492–498. https://doi.org/10.1029/jc087ic01p00492
- Syvitski, J. P., Peckham, S. D., Hilberman, R., & Mulder, T. (2003). Predicting the terrestrial flux of sediment to the global ocean: A planetary perspective. Sedimentary Geology, 162(1–2), 5–24. https://doi.org/10.1016/s0037-0738(03)00232-x
- Williams, M. E., & Stacey, M. T. (2016). Tidally discontinuous ocean forcing in bar-built estuaries: The interaction of tides, infragravity motions, and frictional control. *Journal of Geophysical Research: Oceans*, 121(1), 571–585. https://doi.org/10.1002/2015jc011166
- Wong, S. H., Monismith, S. G., & Boehm, A. B. (2013). Simple estimate of entrainment rate of pollutants from a coastal discharge into the surf zone. Environmental Science & Technology, 47(20), 11554–11561. https://doi.org/10.1021/es402492f
- Zheng, P., Li, M., van der Zanden, J., Wolf, J., Chen, X., Wang, C., et al. (2017). A 3d unstructured grid nearshore hydrodynamic model based on the vortex force formalism. *Ocean Modelling*, 116, 48–69. https://doi.org/10.1016/j.ocemod.2017.06.003

FLORES ET AL. 12 of 12